Mars-solar wind interaction: LatHyS, an improved parallel 3-D multispecies hybrid model

Ronan Modolo, Sebastien Hess, Marco Mancini, François Leblanc, Jean-Yves
Chaufray, David Brain, Ludivine Leclercq, Rosa Esteban Hernandez, Gérard
Chanteur, Philippe Weill, et al.

Mars-solar wind interaction: LatHyS, an improved parallel 3-D multispecies hybrid model

Ronan Modolo[1], Sebastien Hess[1,2], Marco Mancini[1,3], Francois Leblanc[4], Jean-Yves Chaufray[4], David Brain[5], Ludivine Leclercq[1], Rosa Esteban-Hernández[4], Gerard Chanteur[6], Philippe Weill[4], Francisco González-Galindo[7,8], Francois Forget[8], Manabu Yagi[4,9], and Christian Mazelle[1,10]

[1]LATMOS/IPSL, UVSQ Université Paris-Saclay, UPMC University Paris CNRS, Guyancourt, France, [2]ONERA, Toulouse, France, [3]LUTH, Observatoire de Paris, Meudon, France, [4]LATMOS/IPSL, UPMC University Paris 06 Sorbonne Universités, UVSQ, CNRS, Paris, France, [5]LASP, University of Colorado Boulder, Boulder, Colorado, USA, [6]LPP, Ecole Polytechnique, Palaiseau, France, [7]IAA, Granada, Spain, [8]LMD/UPMC/CNRS, Paris, France, [9]Planetary Plasma and Atmospheric Research Center, Graduate School of Science, Tohoku University, Miyagi, Japan, [10]IRAP, Toulouse, France

Abstract In order to better represent Mars-solar wind interaction, we present an unprecedented model achieving spatial resolution down to 50 km, a so far unexplored resolution for global kinetic models of the Martian ionized environment. Such resolution approaches the ionospheric plasma scale height. In practice, the model is derived from a first version described in Modolo et al. (2005). An important effort of parallelization has been conducted and is presented here. A better description of the ionosphere was also implemented including ionospheric chemistry, electrical conductivities, and a drag force modeling the ion-neutral collisions in the ionosphere. This new version of the code, named LatHyS (Latmos Hybrid Simulation), is here used to characterize the impact of various spatial resolutions on simulation results. In addition, and following a global model challenge effort, we present the results of simulation run for three cases which allow addressing the effect of the suprathermal corona and of the solar EUV activity on the magnetospheric plasma boundaries and on the global escape. Simulation results showed that global patterns are relatively similar for the different spatial resolution runs, but finest grid runs provide a better representation of the ionosphere and display more details of the planetary plasma dynamic. Simulation results suggest that a significant fraction of escaping O^+ ions is originated from below 1200 km altitude.

1. Introduction

Since the sixties several planetary missions have explored the neutral and ionized environment of Mars and have led to a comprehensive picture of Mars' atmosphere/ionosphere/solar wind coupling. The interaction of the solar wind with Mars clearly contributes to the erosion of the gaseous envelop and has potentially an important impact on the atmospheric evolution of the planet. The electromagnetic coupling with the Martian atmosphere takes place through ionization processes: ionization by solar photons, electron impact ionization (incident plasma electrons ionize the upper atmosphere), and charge exchange between ionized and neutral particles producing a cold ion and a fast neutral. Due to the supermagnetosonic nature of the solar wind, the interaction region is preceded by a collisionless bow shock (BS) which decelerates, heats, and compresses the solar wind, thereby allowing the incident plasma to flow around the obstacle. Gradually, as the solar wind flow approaches the Martian ionosphere, more and more planetary ions are picked up by the flow. This mass loading of the solar wind contributes to the loss of momentum of the incident flow. Moreover, because the ionosphere is a conductive layer, its interaction with the solar wind induces a pileup and a twist of the interplanetary magnetic field lines around the planet. This region is called the induced magnetosphere and is mainly populated by planetary ions. This simple picture is more complex due to the presence of highly localized remanent magnetic field sources, discovered by Mars Global Surveyor [*Acuna et al.*, 1999]. The characterization of the induced magnetosphere have been accomplished by several recent space missions, in particular, by Mars Global Surveyor [*Albee et al.*, 2001] or Mars Express [*Chicarro et al.*, 2004]. Since September 2014, the MAVEN spacecraft has been observing the Martian upper atmosphere and its interaction with the solar wind [*Jakosky et al.*, 2015]. One of the main goals of the mission is to determine the role that loss to space of volatiles from the Mars atmosphere has played along Mars' history. Reviews of our pre-MAVEN knowledge of the Mars-solar wind interaction and atmospheric escape are summarized in *Lillis et al.* [2015].

Modeling efforts have been conducted to support the analysis of in situ measurements and to understand the impact of specific parameters (solar EUV, dynamic pressure, etc.) on the Martian environment. Global simulation models of Mars' interaction with the solar wind have been developed with various formalisms since the 1980s. One of the first models used a magnetogasdynamic approach [*Spreiter and Stahara*, 1980]. Since then, more sophisticated models have been developed with different formalisms such as multispecies MHD [e.g., *Ma et al.*, 2002, 2004; *Ma and Nagy*, 2007; *Terada et al.*, 2009; *Ma et al.*, 2014], multifluid MHD [e.g., *Harnett and Winglee*, 2006; *Najib et al.*, 2011; *Riousset et al.*, 2013; *Dong et al.*, 2014, 2015a, 2015b], and hybrid models [e.g., *Modolo et al.*, 2005, 2006, 2012; *Kallio et al.*, 2010; *Brecht and Ledvina*, 2010; *Bößwetter et al.*, 2007]. Another approach is to use test particle models to study the properties and the dynamic of a specific ion population [e.g., *Chaufray et al.*, 2007; *Fang et al.*, 2010; *Curry et al.*, 2013, 2015; *Poppe and Curry*, 2014]. All these models are able to characterize the plasma dynamic and the electromagnetic field behavior in the Martian ionized environment as well as the solar wind interaction with the upper atmosphere and the induced ion escape rate estimates.

A three-dimensional multispecies hybrid model dedicated to the description of the plasma dynamic induced by Mars' interaction with the solar wind was developed few years ago [*Modolo et al.*, 2005, 2006]. This approach, based on a kinetic description of the ions and a fluid description of the electrons, takes into account self-consistently the Hall term which breaks the symmetry of the system. The model developed by *Modolo et al.* [2005, 2006] is the only model to involve self-consistently the alpha particles of the solar wind. This allowed *Chanteur et al.* [2009] to estimate the contribution of the solar wind helium balance of the Martian atmosphere. In addition, hybrid approaches include Larmor radii effects which are expected to become important at high altitudes and allow as an example the description of the oxygen plume along the motional electric field direction ($\mathbf{E} = -\mathbf{v} \times \mathbf{B}$). Computational resources for the hybrid approach usually constrain the simulation spatial resolution.

Recently, a modeling effort has been undertaken to improve the spatial resolution of the hybrid model as well as the ionospheric description leading to the LatHyS (Latmos Hybrid Simulation) model. This manuscript reports on the technical developments to parallelize the simulation code and describes the specific improvements of the ionospheric description.

This new version of the simulation model has been used to investigate the solar wind interaction with Mercury [*Richer et al.*, 2012], the Jovian plasma- Ganymede interaction [*Leclercq et al.*, 2016] and the interaction between a magnetic cloud and a terrestrial magnetosphere [*Turc et al.*, 2015].

In parallel, an international modeling team supported by the International Space Science Institute at Bern, Switzerland, focused on intercomparison between models and observations. This global model challenge leads to the first community-wide effort to compare global plasma interaction models for Mars [*Brain et al.*, 2010]. This effort highlights new topics as the role of the hot exosphere on plasma escape and its impact on the interaction region. In addition, discrepancies between results of different models were identified and explained by slightly different inputs or boundary conditions inherent to each model. A new challenge has been undertaken and three simulations, namely, RUN A, RUN B, and RUN C, were performed by the different modeling teams, with more specification concerning the neutral atmosphere, the ionosphere, and the extended exosphere. These three runs are expected to give more information on the influence of the extended exosphere and the EUV flux on the Martian ionized environment.

In this paper, we present these runs as realized by LatHyS code and address the following questions:

1. What is the importance of the extended exosphere on plasma escape?
2. What is the role of the solar EUV radiation on controlling the structure of the interaction region and plasma escape?
3. How are simulation results sensitive to the spatial resolution?

Section 2 describes the hybrid formalism, the parallelization, and the performance of the code. The description of the neutral environment, the ionosphere, and the input parameters are presented in section 3. Global simulation results, the impact of a "hot" exospheric component and of the solar EUV flux on the Martian boundary, and the global escape rate are discussed in section 4.

2. Simulation Model

To study the interaction between an incident plasma and a planetary object, the most complete approach consists in determining the evolution of the distribution function of each species "s" of the plasma $f_s(\mathbf{x}, \mathbf{v}, t)$ governed by the Vlasov equation and the electromagnetic field determined self-consistently from Maxwell's equations. Due to limitations of the computational resources, this approach is usually not applicable to three-dimensional fully kinetic models. The simplest mathematical formalism used is an ideal MHD model which describes the plasma as a single nonresistive fluid coupled to the Faraday's equation. An intermediate approach, between fully kinetic and MHD models, consists of representing the electron as a fluid while ions are described using a kinetic formalism. This approach, although more binding in terms of computational resources than a fluid model, is based on less assumption and include more physics (Hall term, Larmor radius effect, etc.). A complete review of these formalisms, their respective assumptions and limitations are detailed in *Ledvina et al.* [2008], *Kallio et al.* [2011], and *Winske et al.* [2003].

2.1. Hybrid Formalism

Hybrid models are able to describe physical phenomena at ion scales, beyond the scope of MHD. In a hybrid model, electrons are treated as an inertialess fluid, contributing to electric current and enforcing the neutrality of the plasma, while a kinetic description is adopted for the ions. Ions are therefore represented by individual particles called macroparticles. A macroparticle does not represent one ion but a cloud of ions with a given density and with the same properties (ions with the same charge, mass, velocity, and origin). The position and velocity of a macroparticle "j" obey the laws for the motion of physical particles:

$$\frac{d\mathbf{x}_j}{dt} = \mathbf{v}_j \tag{1}$$

$$m_j \frac{d\mathbf{v}_j}{dt} = q_j(\mathbf{E} + \mathbf{v}_j \times \mathbf{B}) - \mathbf{F}_c \tag{2}$$

where q_j and m_j are the charge and the mass of the particle "j", respectively, and $\mathbf{x}_j$ and $\mathbf{v}_j$ the position and velocity of the particle, respectively. $\mathbf{F}_c$ is a drag force exerted by the atmosphere on the charged particle; it describes the ion-neutral elastic collisions. We consider the effect of collisions as friction in the equation of motion. The expression of the drag force on the particle "j" is $\mathbf{F}_c = m_j \nu_{in}(\mathbf{v}_j - \mathbf{u}_n)$, with $\mathbf{u}_n$ the velocity of the neutral targets that we assume to be at rest in the planetary frame ($\mathbf{u}_n = \mathbf{0}$) and ν_{in} is an average ion-neutral collision frequency for momentum transfer [*Banks and Kockarts*, 1973]. The elastic ion-neutral collision frequency can be approximated by $\nu_{in} = 2.6 \times 10^{-9} n_n(\alpha_0/\mu_A)^{1/2}$ s^{-1} where n_n is the neutral number density in cm^{-3}, μ_A is the ion-neutral reduced mass in atomic units, and α_0 is the atomic polarizability ($\alpha_0 = 0.7910^{-24}$ cm^{-3} for O and $\alpha_0 = 2.63 \times 10^{-24}$ cm^{-3} for CO_2) [*Banks and Kockarts*, 1973]. For simplification we used an average value between O and CO_2 for the atomic polarizability.

The density n_s of particle species "s" is determined from the distribution function

$$n_s(\mathbf{x}, t) = \int f_s(\mathbf{x}, \mathbf{v}, t) d^3v \tag{3}$$

The bulk velocity and the ionic current of species "s" are therefore

$$\mathbf{U_s}(\mathbf{x}, t) = \frac{1}{n_s(\mathbf{x}, t)} \int \mathbf{v} f_s(\mathbf{x}, \mathbf{v}, t) d^3v \tag{4}$$

$$\mathbf{J_s}(\mathbf{x}, t) = q_s n_s(\mathbf{x}, t) \mathbf{U_s}(\mathbf{x}, t) \tag{5}$$

The total ionic current corresponds to the sum of ionic currents of all of ion species ($\mathbf{J_i} = \sum_s \mathbf{J_s}(\mathbf{x}, t) = en_i\mathbf{U}_i$, with n_i the ion number density and $\mathbf{U}_i$ the ion velocity). The total current is

$$\mathbf{J} = \mathbf{J}_e + \mathbf{J}_i \tag{6}$$

The assumption of a massless and charge-neutralizing fluid, for the description of the electrons, leading to $n_e = \sum_s n_s$, implies that the electron plasma oscillations and electron inertial lengths cannot be described. Similar to *Lipatov et al.* [2011], for massless electrons the momentum equation of the electron fluid takes the form of the standard generalized Ohm's law [e.g., *Braginskii*, 1965].

$$\mathbf{E} = -\frac{\mathbf{J_e} \times \mathbf{B}}{\rho} - \frac{\nabla p_e}{\rho} - \frac{m_e}{e} \sum_s v_{e,s} \left((\mathbf{U}_i - \mathbf{U}_s) - \frac{\mathbf{J}}{\rho} \right) - \frac{m_e v_{a,e0}}{e} \mathbf{U}_e \qquad (7)$$

where p_e is the scalar electron pressure and $\mathbf{J}_e$ is estimated from equation (6). Like *Lipatov et al.* [2011], in our simulation we assume that $|\mathbf{U}_i - \mathbf{U}_s| \ll J/(ne)$ and we drop the third and the fifth terms from the right side of equation (7). The effective conductivity which appears indirectly in equation (7) is $\sigma_0 = \frac{e^2 n_e}{m_e v_{es}}$ with $v_{es} = 5.4 \times 10^{-10} n_s \sqrt{T_e} \, s^{-1}$ the electron-neutral collision frequency [*Kelley*, 1989]. Even without the presence of an intrinsic magnetic field, the draping and the pileup in the induced magnetosphere lead to magnetic field of the order of several tens of nanoteslas, thus in the upper ionosphere (>150–200 km) $\omega_{ce} = eB/m_e >> v_{en}$, which implies that the parallel conductivity is larger than Pedersen and Hall conductivities. In this case particles have a motion tightly bound perpendicular to $\mathbf{B}$ but are free to move along $\mathbf{B}$. In the lower ionosphere (where $n_e > 1000 \, \text{cm}^{-3}$) a perfectly conducting ionosphere is assumed with $v_i - v_e = 0$.

The time evolution of the magnetic field results from Faraday's equation, meanwhile satisfying the solenoidal condition:

$$\frac{\partial \mathbf{B}}{\partial t} = -\nabla \times \mathbf{E} \qquad (8)$$

$$\nabla \cdot \mathbf{B} = 0 \qquad (9)$$

Since electrons are treated as a fluid, a closure equation is required. Different assumptions can be made on the electron temperature, usually a simple adiabatic law, but more elaborated models can also solve an energy equation for electrons. Since solar wind and ionospheric electrons have different temperatures (10–100 eV for the solar wind electrons, 0.1–10 eV for ionospheric electrons), this model involves two electron fluids, one for solar wind ($n_{e,sw}$) and one for ionospheric ($n_{e,i}$) electrons [*Modolo and Chanteur*, 2008; *Simon et al.*, 2006]. Solar wind and ionospheric electron densities are determined from the solar wind ion densities ($n_{e,sw} = \sum_{k=sw} n_k$) and from the ionospheric ion densities ($n_{e,i} = \sum_{k=iono.} n_k$), respectively. The solar wind electron population is assumed to follow an adiabatic behavior, while ionospheric electron follows a polytropic equation with index varying between 0 (isobaric process) and 5/3 (adiabatic process). The variation of the polytropic index depends upon the electron density, and therefore, it allows going smoothly from a deep ionosphere region where a barotropic ionosphere is assumed to a solar wind region, where an adiabatic behavior is expected. Without this varying polytropic index, the electronic gradient pressure force could act inward and outward, respectively, below and above the ionospheric peak and could contribute to diffuse and extend the ionospheric region.

2.2. Numerical Scheme

Hybrid codes are numerical models which resolve the temporal evolution of the plasma described by a set of discrete equations equivalent to a Vlasov system. The most used algorithms for plasma-celestial bodies interaction are the *Harned* [1982] scheme, the *Kallio and Janhunen* [2001], and the *Matthews* [1994] schemes.

In this model, $\mathbf{E}$ and $\mathbf{B}$ are computed on two identical grids interleaved by half a grid cell in all directions to ensure a divergence-free magnetic field at second-order approximation [*Birdsall and Langdon*, 2004]. This is a common feature to many electromagnetic codes. The magnetic field, the density, the electron pressure, ionic currents, and other momenta are computed at each corner of the cell of the B grid (in reference to the magnetic field). The electric field is defined at the corner of the cell of the E grid, which corresponds to the center of the cell of the B grid. Such shifted B and E grids allow an optimal computation of rotational and gradients that appear in Maxwell equations. The $\nabla \times \mathbf{E}$ is located at the same position as $\mathbf{B}$ and is accurate to the second order in Δx. Reciprocally, $\nabla \times \mathbf{B}$ and ∇P_e are computed on the E grid.

Ions are described by a set of macroparticles. Each macroparticle has the volume and the shape of a numerical cell (see *Leclercq et al.* [2016] for details). The position of the macroparticle is identified by its center of mass.

Charge density and ionic current at a given grid point (x_k) are defined by the position and the speed of the macroparticles via the following expressions:

$$\rho_k = \sum_s \phi_k(\mathbf{x_s})q_s \tag{10}$$

$$\mathbf{J}_k = \sum_s \phi_k(\mathbf{x_s})q_s\mathbf{v}_s \tag{11}$$

$\phi_k(\mathbf{x_s})$ represents the contribution of the macroparticle s, with its center located at $\mathbf{x}_s$, to the grid point k. A common cloud-In-cell technique is used to determine the contribution of the macroparticle to density and currents on the grid points [*Birdsall and Langdon*, 2004].

To determine the electric and magnetic fields seen by the macroparticles, we use the same interpolation technique in order to avoid artificial forces exerted by the grid on the particles [*Birdsall and Langdon*, 2004].

A common leapfrog scheme is used to push particles. The core of the present hybrid model is based on the Current Advance Method and Cyclic Leapfrog algorithm designed by *Matthews* [1994], now frequently referred as CAMCL. This latter reference gives a detailed description of the CAMCL algorithm and of its validation tests. The CAMCL kernel has been redesigned for the modeling of planetary environments [*Modolo et al.*, 2005; *Modolo and Chanteur*, 2008; *Richer et al.*, 2012; *Leclercq et al.*, 2016]. First, variable statistical weights of macroparticles were implemented to enable a large range of physical densities extending over more than six decades [*Modolo and Chanteur*, 2008]. Second, sources and sinks of particles and open boundary conditions were defined and adapted either to subsonic or supersonic flows of the external plasma. Third, the simulation code was parallelized as briefly described in section 2.3.

The macroparticle weight is proportional to the number of physical ions represented by the macroparticle. When a new macroparticle is created through one of the physical production processes, its weight can be rather large, especially in the ionospheric region. If one of these "heavy" macroparticles reaches the low-density region, it might contribute to increase the numerical noise in the simulation due to the inherent limited statistics of this approach. To solve this issue a splitting technique has been implemented. When a numerical particle with a statistical weight larger than the weight corresponding to 3 times the solar wind density reaches a distance from the obstacle larger than a given value (700 km in the presented results), the macroparticle is split in two daughter particles which have half of the statistical weight of the parent particle. Daughter particle conserves the same identity and the same speed as the parent particle. The positions of the new particles are shifted by a small random distance $\pm\Delta s$ from the original particle position. This random distance is such that $\Delta s < 5 \times 10^{-3}\Delta x$ with Δx as the spatial step of the simulation. Therefore, the mass center is exactly conserved during the splitting process. This very small random distance ensures the continuity of particle trajectory, but the two daughter particles will get a slightly different acceleration due to cloud-in-cell interpolation technique, and their trajectory will start diverging after few time steps.

2.3. Parallelization and Performance
Sequential simulation codes, i.e., those which are executed on a single processor and treat instructions one by one, are the simplest in terms of programming effort but present few drawbacks. Performances of these sequential models are linked to the available computational CPU characteristics. For kinetic simulations, hybrid, or full particle-in-cell, the number of numerical particles are the main driver for the memory requirements of a simulation. Since the number of particles is proportional (at the first order) to the number of cells, we can quickly reach the limits of the available resources (the memory associated to a single processor) when reducing the spatial resolution. In addition, the computational time increases with the number of particles leading to simulations which can last several weeks on a single processor. To overcome these constraints and to better optimize the simulation model, a parallelization effort was undertaken. The best known approaches are as follows: (i) OpenMP a multitask parallelization software for shared memory machines (presence of many cores on a single node), (ii) MPI software, parallelization by exchange of messages for distributed memory machines (cluster servers/nodes), and (iii) the parallelization on graphics card (using coprocessors on GPU graphics cards to deport calculation of the node). LatHyS makes use of MPI [*Message Passing Interface Forum*, 2012].

2.4. Domain Decomposition
The domain decomposition method is widely used in parallelization and is well adapted to distributed memory and parallel architectures. It decomposes the simulation domain into subdomains with as many

subdomains as processes. Each subdomain is associated to a unique process. The number of subdomains, their dimensions, depend on the number of processes used for the simulation run. Information found at the subdomain interfaces are operated through communications between processes (physical or virtual) sharing these interfaces, because in our approach the X axis corresponds to the direction of the incoming plasma flow; the topology of the domain decomposition is two dimensional and lies within the YZ plane of the simulation in order to minimize the number of communications.

Each process will realize the calculations in its subdomain for both fields and particles. Processes are grouped into communicators which allow exchange of messages to a certain group of processes. In the simulation model, two communicators are defined and used for exchange messages: one for periodic boundary conditions and a second one for open boundary conditions. Boundary conditions are detailed in section 3.4.2.

2.5. Individual and Collective Communications

Individual communications or point-to-point communications are used to exchange information between two processes, while collective communications allow a process to send this information to all processes belonging to the same communicator. Collective communications are used to distribute global information such as the total number of particles or the total magnetic energy of the simulation. Point-to-point communications represent the vast majority of send/receive directives made during a run and are neighborhoods communications, that is to say, between a process and its eight neighbors. These communications are involved in the management of particles and interfaces between subdomains associated to processes.

2.5.1. Managing Particles

At each time step, each process "pushes" particles of its subdomain. It is then necessary to identify the particles that leave the subdomain and to determine their new subdomain. The exchange of messages is performed in two steps. First, each process tags and informs all receiver subdomains about the number of particles they will receive and from which process. This step allows to prepare the reception of particles by allocating memory space for the data to be exchanged.

The second step consists in sending information about transferred particle (position, velocity, charge, mass, origin, etc.) to the destination process. This information is collected in a structure created specifically for this purpose. Different communicators are used depending upon the origin of the particle (solar wind or ionospheric) and their associated boundary conditions.

2.5.2. Managing Interfaces Between Subdomains

Fields and moments calculations are determined on mesh nodes. Grid points may be therefore common to several subdomains if they are located on the interfaces between two subdomains.

A particular attention is paid to the calculation of ion moments and currents. At grid points located on interfaces, since ion moment and current contributions are determined from particles within the subdomain, thus particle contributions from neighboring subdomains cannot be taken into account. To solve this problem, processes add the contributions to the ion moments and current of neighbor subdomains for all interface grid points.

2.6. Performance

The parallelized simulation code has been tested, validated, and is currently used on a mesoscale computational platform: CICLAD (http://ciclad-web.ipsl.jussieu.fr/accueil/). The platform server is based on a x86−64 architecture and each node is interconnected by infiniband cables. A common task in High Performance Computing (HPC) is to determine the performances of the simulation model. A scalability test has been performed, and we have simulated the propagation of a free solar wind in the simulation domain for different numbers of CPUs and measured the performance enhancement, i.e., the speedup.

In our test, the problem size stays fixed but we increased the number of processing elements; it refers to the strong scaling case. The strong scaling efficiency is determined by the ratio between the amount of time t_1 to complete the work and the amount time t_p needed to complete the work on p processing element. Strong scaling efficiency is given by

$$S(p) = \frac{t_1}{t_p \times p}$$

where p is the number of processors used for parallel simulation. In strong scaling, ideally, a program should scale linearly. In general, it is harder to achieve good strong scaling at larger process counts since the communication overhead for many/most algorithms increases in proportion to the number of processes used.
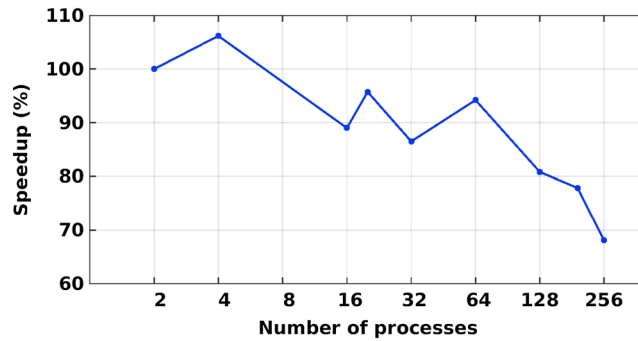
Figure 1. Parallel speedup of the code. The blue curve shows the real performance.)

Figure 1 displays the performance of the code showing a relatively good behavior of the parallelization scheme.

3. The Martian Simulation Model

3.1. The Neutral Environment

The Martian neutral environment is described as a one-dimensional radial density profile of CO_2, H, and O which are displayed in Figure 2. Information concerning the neutral environment is based on inputs from the international team of the Solar Wind Model Challenge at the International Space Science Institute (ISSI) in Bern, [*Brain et al.*, 2010] and are available at http://www.issibern.ch/teams/martianplasma/. Atmospheric density profiles are partly derived from the Mars thermosphere global circulation model (MTGCM) [*Bougher et al.*, 2000, 2006, 2008], except for the atomic hydrogen corona, assuming a spherically symmetric neutral environment. Three simulations, noted RUN A, RUN B, and RUN C, have been performed and represent different states of the Martian neutral environment, for solar minimum (RUN A and RUN B) and maximum (RUN C). RUN A describes only the "cold" population, i.e., the thermal component of the atomic hydrogen and oxygen of the thermosphere, while RUN B (like RUN C) combines both the "cold" and the "hot" populations for these two neutral species. Thermospheric profiles are based on the MTGCM which was run for Ls = 270, $F_{10.7} = 34$ at Mars for RUN A and RUN B, while RUN C was based on results for Ls = 270, $F_{10.7} = 105$ at Mars. Profiles of the "hot" oxygen corona are based on *Valeille et al.* [2010] results. O and CO_2 profiles have been fitted from MTGCM results by a combination of exponential terms:

$$n_X(z) = n_1 \exp(-z/h_1) + n_2 \exp(-z/h_2) + n_3 \exp(-z/h_3) + n_4 \exp(-z/h_4) + n_5 \exp(-z/h_5) \qquad (12)$$

where z is the altitude (in km), n_i and h_i represent a reference density and a scale height, respectively (Table 1).
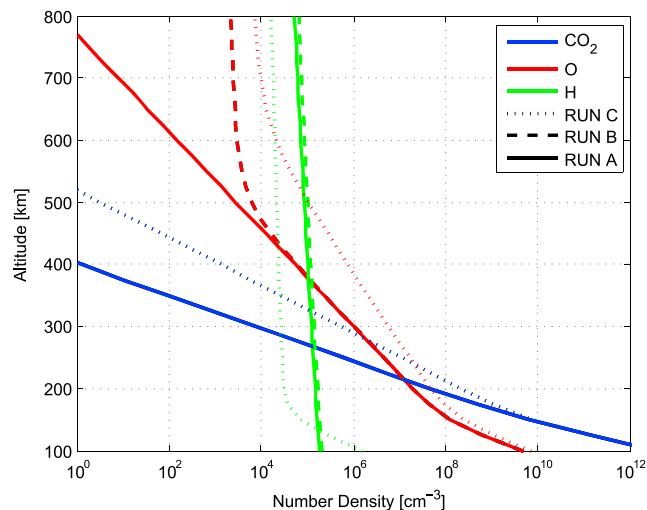

Figure 2. Density profiles for the CO_2 (blue), O (red), and H (green) used in the simulations. Full lines represent the profiles used for RUN A, the dashed lines for RUN B while the dotted lines are for RUN C.

Table 1. Numerical Values of Fitting Parameters of Equation (12) for O and CO_2 Density Profiles[a]

RUN #	"Cold" Population		"Hot" Population		
	(n_1, h_1)	(n_2, h_2)	(n_3, h_3)	(n_4, h_4)	(n_5, h_5)
RUN A (CO_2)	$(6.04e^{18}, 6.98)$	$(1.66e^{15}, 11.49)$	-	-	-
RUN B (CO_2)	$(6.04e^{18}, 6.98)$	$(1.66e^{15}, 11.49)$	-	-	-
RUN C (CO_2)	$(5.88e^{18}, 7.0)$	$(3.55e^{13}, 16.67)$	-	-	-
RUN A (O)	$(5.85e^{13}, 10.56)$	$(7.02e^{09}, 33.97)$	-	-	-
RUN B (O)	$(5.85e^{13}, 10.56)$	$(7.02e^{09}, 33.97)$	$(5.23e^{23}, 626.2)$	$(9.76e^2, 2790.)$	$(3.71e^{14}, 88.47)$
RUN C (O)	$(2.33e^{13}, 12.27)$	$(2.84e^{09}, 48.57)$	$(1.5e4, 696.9)$	$(2.92e^3, 2891.)$	$(5.01e^4, 99.19)$

[a]RUN A does not include a "hot" population.

For hydrogen, the density profile used is a combination of results from *Anderson and Hord* [1971] and *Krasnopolsky* [2002]. Hydrogen profiles in the homosphere and heterosphere have been described by the sum of two exponentials. The first (second) term represents the hydrogen profile below (above) the homopause. For RUN A, we simplified the hydrogen profile by extrapolating at high altitude, above the homopause.

We assume that both hydrogen populations are isothermal fluids in pressure equilibrium in the gravity field of the planet with

$$n_H(z) = n_1 \exp\left(a_1 * \left(\frac{1}{z + 3393.5} - \frac{1}{3593.5}\right)\right) + n_2 \exp\left(a_2 * \left(\frac{1}{z + 3393.5} - \frac{1}{3593.5}\right)\right) \quad (13)$$

where $a_{1,2} = \frac{GM_{Mars}m_H}{k_B T_{1,2}}$ with G the universal gravitational constant, M_{Mars} the mass of the planet, m_H the mass of one hydrogen atom, k_B the Boltzmann constant, and $T_{1,2}$ the temperatures of the "cold" and "hot" populations for subscripts 1 and 2, respectively. The parameter $n_{1,2}$ represents the reference densities at the exobase for each population. Values of the coefficients are given in Table 2.

3.2. Plasma Sources

Photoproduction. Local photoproduction rates of CO_2^+, O^+, and H^+ are calculated by making use of the Extreme UltraViolet flux model for Aeronomics Calculations (EUVAC) developed by *Richards et al.* [1994] and taking into account the atmospheric photoabsorption. EUVAC is based on a reference spectrum involving 37 wavelength intervals, covering a range of 5 to 105 nm. Production rates are calculated with the usual expression [see *Schunk and Nagy*, 2004]:

$$q_{X^+}^{photo}(z, \chi) = n_X(z) \int_0^{\lambda_t} \sigma_X^i(\lambda) I_\infty(\lambda) \exp\left[-\tau(z, \lambda, \chi)\right] d\lambda \quad (14)$$

with q_{X^+} the production rate of the ion species X^+, $n_X(z)$ the density of the neutral component X at the altitude z, σ_X^i the ionization cross section of the species X, I_∞ the nonattenuated solar EUV flux calculated with the EUVAC model [*Richards et al.*, 1994], and τ the optical depth. The optical depth $\tau(z, \lambda, \chi)$, specifies the attenuation of the solar irradiance by the atmosphere. It is defined as

$$\tau(z, \lambda, \chi) \equiv \int_\infty^z \sum_s n_s(z) \sigma_s^a(\lambda) \sec \chi \, dz \quad (15)$$

where σ_s^a are the absorption cross sections, χ is the solar zenith angle, and index s corresponds to the two main neutral species of interest (CO_2 and O). Note that this expression of the optical depth is valid for $\chi < 75°$. Above

Table 2. Numerical Values of Fitting Parameters of Equation (13) for Atomic H Density Profile[a]

RUN #	"Cold" Population	"Hot" Population
	(n_1, a_1)	(n_2, a_2)
RUN A	$(1.5e^5, 2.5965e^4)$	–
RUN B	$(1.5e^5, 2.5965e^4)$	$(1.9e^4, 1.0365e^4)$
RUN C	$(1.e^3, 9.25e^5)$	$(3.e^4, 1.48e^4)$

[a]RUN A does not include a "hot" population.

Table 3. Coefficients of Electron Impact Ionization (H^+ and O^+)

Frequency (cm^3 s^{-1})	A_0	A_1	A_2	A_3	A_4
ν_{H^+}	−1143.33	323.767	−35.0431	1.69073	−0.0306575
ν_{O^+}	−1233.29	347.764	−37.4128	1.79337	−0.0322777

this limit the full expression of the optical depth defined by *Rees* [1989] has been used. The photoabsorption by the atmosphere of the planet is computed from the radial profiles of the neutral species CO_2 and H and using photoabsorption cross sections given by *Schunk and Nagy* [2004]. Photoproduction calculations are computed consistently with the neutral MTGCM simulations, i.e., with an $F_{10.7}$ index of 34 (at Mars) for RUN A and RUN B, and an $F_{10.7}$ index of 105 for RUN C. Indeed, the EUVAC model requires a daily $F_{10.7}$ and an 81 day average, for each run we used identical daily averaged values.

Electron impact ionization. When the energy of the electrons is large enough (above the ionization threshold of the neutral atom or molecule), the neutral species can be ionized through collisions with electrons either directly

$$X + e^- \longrightarrow X^+ + e^- + e^- \tag{16}$$

or by auto-ionization after excitation

$$X + e^- \longrightarrow X^* + e^- \tag{17}$$

$$X^* \longrightarrow X^+ + e^- \tag{18}$$

Total cross sections of atoms and molecules by electron impact are available at the National Institute of Standards and Technology [*Kim et al.*, 2004]. Ionization cross sections by electron impact of O and H have been used to determine the ionization frequency. The electronic impact frequency is computed from [*Cravens et al.*, 1987]

$$\nu_{X^+}^e(T_e) = n_e \int_0^\infty v\sigma(v) f(v, T_e) 4\pi v^2 \mathrm{d}v \tag{19}$$

Assuming that the electron distribution function is Maxwellian and isotropic, this hypothesis might be inadequate in certain cases, particularly downstream of a collisionless bow shock where the electronic distribution function appears to be a flat-topped function. The electron impact coefficient rate $\nu^e(T_e)$ can be represented by an exponential function with polynomial terms in the exponent:

$$\nu_{X^+}^e(T_e) = \exp\left(A_0 + A_1 \cdot x + A_2 \cdot x^2 + A_3 \cdot x^3 + A_4 \cdot x^4\right) \tag{20}$$

where $x = \ln(T_e)$ and A_i are fitted coefficients. These coefficients are listed in Table 3. Thus, the production rate of a given species by electron impact ionization is

$$q_{X^+}^e = \nu_{X^+}^e n_X \tag{21}$$

Charge exchange. Charge exchange reactions are not strictly speaking production processes since no new electrons are produced and the momentum of the incident ion is just kept by neutralized ion which becomes an ENA (energetic neutral atom). The reaction is

$$X^+ + M \longrightarrow X^{\mathrm{ENA}} + M^+ \tag{22}$$

During this reaction the incident ion X^+ captures an electron from the electronic shell of the neutral M to form an energetic neutral atom X^{ENA} and a cold ion M^+. Only charge exchange reactions from incident protons were considered. Cross sections used are $\sigma_{H^+,H} = 2.5 \times 10^{-15}$ cm^2 and $\sigma_{H^+,O} = 1 \times 10^{-15}$ cm^2 [*Stebbings et al.*, 1964; *Stancil et al.*, 1999]. Although the cross section is almost constant in the range 40 eV–1 keV for nonresonant reactions (e.g., H^+, O), the cross section varies by more than a decade for resonant reactions (e.g., H^+, H). Previous simulation runs taking into account the energy dependency did not show a drastic change in the results; therefore, we keep the cross section constant, as requested from the model challenge conditions.

The charge exchange ionization rate is

$$q_M^{CX} = \sigma_{X^+,M} \times n_M \times n_{X^+} \times v_{X^+} \tag{23}$$

with v_{X^+} the velocity of the incident ion and n_M and n_{X^+} the densities of the neutral M and of the ion species X^+, respectively. To determine which macroparticles will undergo a charge exchange collision, we compute the collision probability of each macroparticle with neutrals.

For each macroparticles, at each time step, we compute the probability for a macroparticle "p" to have a free flight (without charge exchange collision) within a volume with a density n_M over a time larger or equal to Δt (the time step). This probability is

$$\mathcal{P}_{p,M} = \exp\left(-\sigma_{X^+,M} \times n_M \times v_p \times \Delta t\right) \qquad M = H,O \tag{24}$$

Therefore, the probability to have a collision during the time step Δt is

$$\mathcal{P}_{coll.\,p} = 1 - \Pi_{M=H,O}\mathcal{P}_{p,M} \tag{25}$$

To determine if a macroparticle undergoes a charge exchange, a random number is drawn. If the probability to have a collision is larger than the random number, then the charge exchange is realized and the parent macroparticle (X^+), i.e., the whole cloud of physical ions, is neutralized and replaced by a daughter macroparticle (M^+) with the same weight, i.e., the same number of physical particles, at rest in the frame of the planet. The daughter macroparticle can represent either H^+ or O^+ ions. To determine which ion species will be represented by the macroparticle, we compute their relative probability of collision.

$$\mathcal{P}_M = \frac{1 - \mathcal{P}_{p,M}}{\sum_{X=O,H}(1 - \mathcal{P}_{p,M})}\mathcal{P}_{coll.\,p}, \qquad M = H,O \tag{26}$$

If the random number is in the interval $[0, \mathcal{P}_H]$ the daughter macroparticle will represent H^+ ions, while if the random number is in the interval $[\mathcal{P}_H, \mathcal{P}_H + \mathcal{P}_O]$ the daughter macroparticle will represent O^+ ions.

3.3. The Ionospheric Model

Obviously a 3-D global kinetic model, with a domain size of several Mars radius and a uniform spatial resolution, is not suited to describe the ionospheric dynamic in detail. The 1-D and 3-D ionospheric models [*Krasnopolsky*, 2002; *Fox*, 2009; *González-Galindo et al.*, 2013] which have a much better spatial resolution and a complete description of the ionospheric chemistry are more appropriate. A first approach used by several global models [*Ma et al.*, 2004; *Brecht and Ledvina*, 2010; *Dong et al.*, 2015a] is to simplify the ionospheric description and limit the chemical reactions to the most important ones. We focus on the two main neutral species of the Martian atmosphere (CO_2 and O) below the exobase level (~200 km height), the three major ion species (O_2^+, CO_2^+, and O^+) and the main associated chemical reactions [*Krasnopolsky*, 2002].

The most important reactions included in this model are listed in http://www.issibern.ch/teams/martianplasma/ and reported in Table 4 with their coefficient rates and column rates. For an ion species i with number density n_i, product ion rate Q_i, loss rate L_i and velocity v_i, the continuity equation is

$$\frac{\partial n_i}{\partial t} + \nabla(n_i v_i) = Q_i - L_i \tag{27}$$

Photochemistry dominates at low altitude (<200 km) in the Martian dayside ionosphere, while transport starts to become effective around 250–300 km [*Chaufray et al.*, 2014]. The transport term in equation (27) can therefore be neglected in the lower ionosphere, which leads to production terms

$$\begin{cases} q_{CO_2^+} = \frac{\partial n[CO_2^+]}{\partial t} = k_1 n[CO_2] - k_4 n[CO_2^+]n[O] - k_5 n[CO_2^+]n[O] \\ q_{O^+} = \frac{\partial n[O^+]}{\partial t} = k_2 n[CO_2] + k_3 n[O] + k_5 n[CO_2^+]n[O] - k_6 n[O^+]n[CO_2] \\ q_{O_2^+} = \frac{\partial n[O_2^+]}{\partial t} = k_4 n[CO_2^+]n[O] + k_6 n[O^+]n[CO_2] - k_7 n[O_2^+]n_e \end{cases} \tag{28}$$

The k_i coefficients correspond to rate coefficients of the chemical reaction number i. The parameters k_1, k_2, and k_3 are photoproduction rates taking into account photoabsorption. During the simulation we compute

Table 4. Reactions, Their Rate Coefficients in $cm^{-3} s^{-1}$ and Column Rates According to *Krasnopolsky* [2002] and *Ma et al.* [2004][a]

Reaction Number	Reaction Equation	Coefficient Rates	Column Rate
1	$CO_2 + h\nu \longrightarrow CO_2^+ + e$	$\lambda < 902$ Å	$1.24e^{+10}$
2	$CO_2 + h\nu \longrightarrow O^+ + CO + e$	$\lambda < 650$ Å	$1.09e^{+9}$
3	$O + h\nu \longrightarrow O^+ + e$	$\lambda < 911$ Å	$1.20e^{+8}$
4	$H + h\nu \longrightarrow H^+ + e$	$\lambda < 911$ Å	$1.00e^{+5}$
5	$CO_2^+ + O \longrightarrow O_2^+ + CO$	$1.64e^{-10}$	$8.07e^{+9}$
6	$CO_2^+ + O \longrightarrow O^+ + CO_2$	$9.6e^{-11}$	$4.72e^{+9}$
7	$O^+ + CO_2 \longrightarrow O_2^+ + CO$	$1.1e^{-9}$	$6.28e^{+9}$
8	$O_2^+ + e \longrightarrow O + O$	$1.95e^{-7}(300/T_e)^{0.7}$	$1.36e^{+10}$
9	$CO_2^+ + e \longrightarrow CO + O$	$3.5e^{-7}(300/T_e)^{0.5}$	$7.52e^{+9}$

[a]Column rates are in $cm^{-2} s^{-1}$, corrected for radius, i.e., multiplied by $(1 + r/r_0)^2$, and refer to medium solar activity.

the production in the ionospheric region according to equation (28). If the production term (for a given cell) is positive, we add one macroparticle in the simulation with a numerical weight appropriate to represent the number of physical ions produced in the volume of the cell during one time step and a zero velocity. In case of a negative production term, a very rare event, we do not remove macroparticles.

Implementation of the ionosphere at initialization. At initialization, we assume that the ionosphere is in photochemical equilibrium (stationary ionosphere and no transport). From these two assumptions we can use equation (27) to compute the ion density profiles. We load judiciously macroparticles in the simulation to reproduce these ion density profiles (up to 450 km height). We initialize uniformly the whole simulation, including the ionospheric region, box with a solar wind plasma (to keep the procedure simple). After the initial loading the motion of the ionospheric particles is inhibited during the first $50 \, \Omega_{H^+}^{-1}$ (about 2500 time steps): this allows the solar wind plasma to start moving around the ionosphere and to develop a bow shock (BS) upstream of the obstacle. Without this initial stage, the simple loading of the macroparticles of the solar wind plasma led to a large convective electric field, close to the ionopause, which removed a significant part of the upper ionosphere. During the simulation, we perform the ionospheric chemistry calculation only in a shell below 350 km height.

Brecht and Ledvina [2012] used a slightly different technique, they introduced a spherical grid where the chemistry is performed on much higher resolution than the Cartesian grid. They preliminarily build up their ionosphere by computing production rates and adding ionospheric macroparticles until they reach a photochemical equilibrium. Second, once the ionosphere has reached equilibrium, they start the advection of the plasma and the evolution of the electromagnetic field. A third technique used by *Kallio et al.* [2010] who implemented a fluid background ionosphere is introduced.

3.4. Solar Wind Plasma, and Initial and Boundary Conditions

Solar wind parameters have the values used for the ISSI challenge and are almost identical to parameters used by *Kallio et al.* [2010], *Brecht and Ledvina* [2010], and case 5 of *Ma et al.* [2004]. The solar wind plasma is characterized by a proton number density of $n(H_{sw}^+) = 2.7$ cm^{-3}, 5% of He^{++} particles, a proton temperature of 13 eV, and a plasma speed of 485 km/s. The interplanetary magnetic field (IMF) is tangential to a Parker spiral in the XY_{MSO} plane with an angle of 56textdegree and a magnitude of 3 nT. Crustal magnetic fields are not included in these simulations.

3.4.1. Initial Conditions

Initially, the computational domain is filled up by ionospheric particle (at rest) and by particles of the supersonic and superalvenic solar wind flow with a homogenous spatial distribution and a Maxwellian distribution function. The magnetic field is loaded uniformly in the simulation, including in the obstacle and the ionosphere, with the IMF magnitude and direction. The electric field at initialization is computed from equation (7) after estimating moments, currents, and electron pressure (equations (4)–(6)). When the simulation begins, we start injecting newborn ions from the different production sources, i.e., photoproduction, electron impact ionization and charge exchange. As already mentioned, the ionospheric production is computed only below 350 km altitude and after $t = 50\Omega_{H^+}^{-1}$.

Table 5. Characteristics of Simulation Runs Performed for This Study

RUN Number	Solar Cycle	"Hot" Corona	Δx (km)
RUN A	Minimum	No	80
RUN B	Minimum	Yes	80
RUN C	Maximum	Yes	80
RUN C2	Maximum	Yes	50
RUN C3	Maximum	Yes	130
RUN C4	Maximum	Yes	180

3.4.2. Boundary Conditions

For particles. Open boundary conditions are used in the X direction at the entry and the exit faces for the solar wind plasma. At the entry of the simulation domain ($X = 2.1R_M$), an ion flux is imposed to preserve the Maxwellian distribution function of the solar wind. The planetary plasma is allowed to leave freely the simulation domain through any of its edges. There is no influx of pickup ions at the side boundaries. On the sides of the simulation box ($Y = \pm4.7R_M$ and $Z = \pm4.7R_M$), periodic boundary conditions are imposed to solar wind macroparticles. Such simple conditions are possible since the sides of the simulation box are far away from the interaction region and the bow shock does not intersect the flank of the simulation domain. The Martian dense atmosphere is considered as a fully absorbing obstacle; particles reaching or penetrating below an altitude of 110 km are stopped but are not removed from the system.

Electromagnetic fields. At the entrance of the simulation domain, the IMF and the convection electric field are imposed. Periodic conditions along Y and Z directions are applied to the electromagnetic fields. Open conditions are used on the exit face ($X = -2.7R_M$). No particular condition on the electromagnetic field is imposed inside the simulation domain.

4. Simulation Results

Six simulation runs have been performed and are summarized in Table 5. Identical solar wind parameters have been used for all simulation runs (section 3.4). Only different solar activities (minimum/maximum), the presence or absence of a "hot" corona or not and the spatial resolution were changed from one simulation to the other.

Simulations have been performed over 18,000 time steps with a particle time step of $\Delta t = 0.03\Omega_{H^+_{sw}}$. It corresponds to about $t = 60T_{transit}$ where $T_{transit}$ is the transit time through the simulation domain (along the X axis) for an undisturbed solar wind particle. The CAM-CL algorithm includes a substepping of the magnetic field, we have chosen $\Delta t_B = \Delta t/4$. The simulation domain is meshed by a 3-D uniform Cartesian grid with a spatial resolution of $\Delta x = 0.6\, c/w_{pi} = 80$ km for RUN A, RUN B, and RUN C. We used $200 \times 386 \times 386$ grid points and about 2.1×10^8 to 3.3×10^8 particles (for RUN A to RUN C). Each of these simulations needed about 80 Gb RAM memory and 13,440 h of cumulative CPU time. For RUN C2, with $\Delta x = 0.375\, c/w_{pi} = 50$ km resolution, the grid size is $320 \times 608 \times 608$, the total number of particles is $\sim1.3 \times 10^9$ particles. It required 325 Gb RAM and 37,355 h (total accumulated CPU time).

For RUN C, Figure 3 displays four 3-D panels which illustrate the magnitude of the magnetic field (Figure 3a), the plasma bulk speed (Figure 3b), the solar wind proton density (Figure 3c), and the planetary O$^+$ ions density (Figure 3d). The 2-D plane cuts of most of the macroscopic parameters for RUN A, RUN B, and RUN C, are provided in the supporting information.

In these simulations, the IMF lies in the XY plane, while the convected electric field points toward the $+Z$ direction. These new simulation results, as in previous simulation results [*Modolo et al.* 2005, 2006], exhibit the main feature of the induced Martian magnetosphere. The BS is clearly visible and identified by an enhancement of the magnitude of the magnetic field (Figure 3a), an increase of solar wind proton density (Figure 3c), and a decrease of the solar wind speed (Figure 3b). Multiple shock-like structures inside the magnetosheath can also be seen. They correspond to signatures of the overshoot of the BS and are due to ion kinetic effects. The thickness of one of these structures is typically $1-3\, c/\omega_{pi}$, which is significantly larger than the spatial resolution $\Delta x = 0.6c/\omega_{pi}$. Additionally, a significant asymmetry of the BS location in the XY plane can be seen and is related to the parallel-perpendicular BS asymmetry. The quasi-parallel BS is closer to the obstacle side
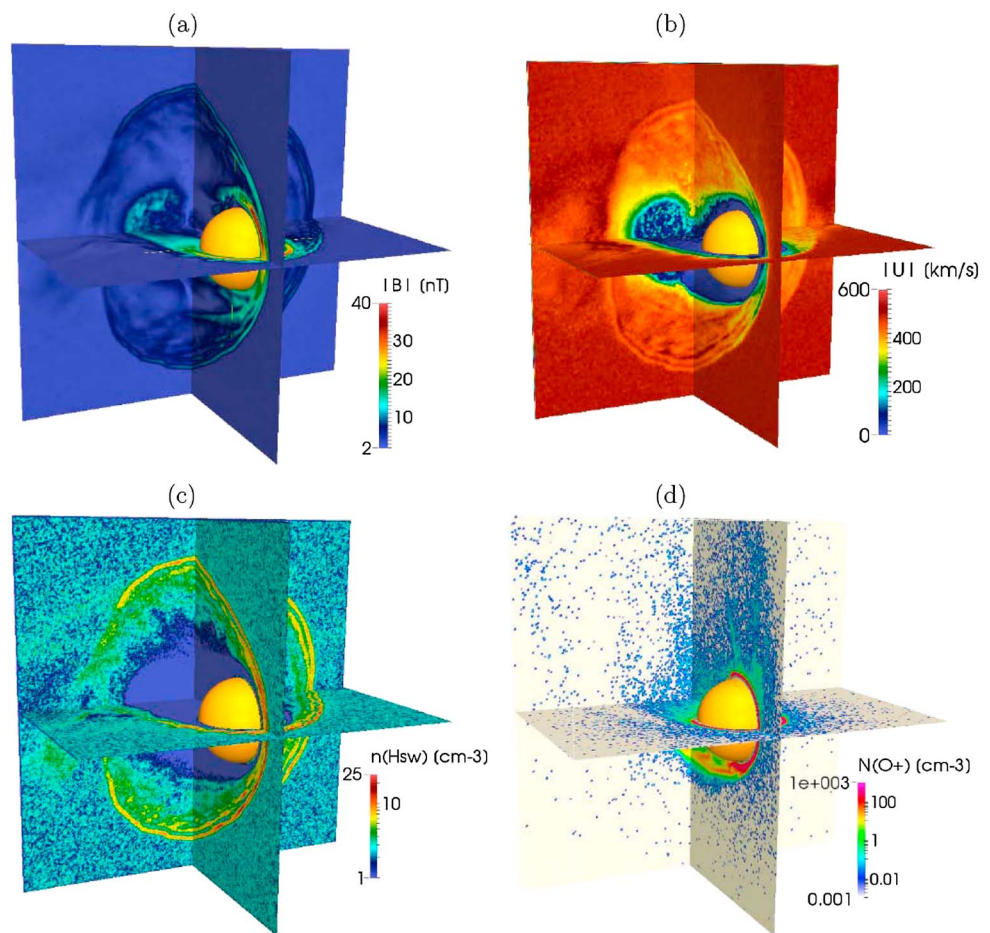
Figure 3. Three-dimensional illustrations of macroscopic parameters computed by our hybrid model. (a) The total magnetic field, (b) the plasma bulk speed, (c) the solar wind proton number density, and (d) O^+ ion number density.

than to the quasi-perpendicular shock, as previously shown by global MHD results [*Ma et al.*, 2004; *Najib et al.*, 2011] and Mars Global Surveyor observations [*Vignes et al.*, 2002]. Closer to the obstacle, a second boundary can be seen on the magnetic and plasma speed figures which corresponds to the Induced Magnetosphere Boundary (IMB) or Magnetic Pileup Boundary (MPB) [e.g., *Bertucci et al.*, 2003; *Lundin et al.*, 2004]. The magnetic pileup upstream of the obstacle occurs with an enhancement of the magnetic field larger than 10 times the IMF which can reach more than 50 nT upstream of the obstacle. At this boundary the ion composition changes upstream in the induced magnetosphere; upstream to the magnetic pileup boundary, the solar wind plasma does not significantly penetrate and this cavity in the solar wind is partially filled by the planetary plasma (Figures 3c and 3d). The induced magnetosphere region is thus governed by planetary plasma, the bulk speed of which being relatively small (<50 km/s).

The *XZ* plane shows a strong asymmetry between the +E and −E hemispheres. Two pathways of planetary O^+ ions escape can be identified in Figure 3d: a plume-like region in the +E hemisphere where iono-spheric/pickup ions are accelerated from the convection electric field away from the planet, and an ion tailward outflow slightly shifted in the −E hemisphere. In this hemisphere, a sharp boundary layer between solar wind and planetary plasma is formed tailward, while on the +E hemisphere solar wind and planetary plasma are much more mixed. Similar results have been found in other Martian global hybrid simulations [*Brain et al.*, 2010] and also in other simulations of plasma-unmagnetized atmosphere interaction [*Simon et al.*, 2006; *Modolo and Chanteur*, 2008]. Multispecies single-fluid MHD models do not predict such asymmetry [e.g., *Ma et al.*, 2004; *Brain et al.*, 2010]. *Simon et al.* [2006] have attributed this asymmetry and the formation of an induced composition boundary to the combined effect of the convection electric field and the electron pressure gradient. In the −E hemisphere, the electric field on the flank of this boundary layer is pointing toward the magnetospheric tail and prevents planetary ions to move outside this region. On the other hand, the

magnetosheath plasma flow is almost tangential to the boundary layer. The resulting electron pressure gradient is then directed inward, so that the solar wind plasma particles cannot move inside the magnetospheric tail by the $-\nabla P_{e,i}$ force [*Simon et al.*, 2006]. In contrast, in the +E hemisphere, the convected electric field points outward of the ionospheric tail and the planetary plasma is efficiently mixed with the shocked solar wind plasma. It increases the mass loading of the solar wind in this region and tends to reduce the plasma speed and the convected electric field. At dayside, the magnetic field maps emphasize a similar asymmetry in the *XZ* plane, the magnetic pileup being stronger in the +E hemisphere. This is induced by the stronger mass-loading effect of the solar wind which reduces the plasma bulk speed and the total electric field. Such an asymmetry has been observed by MGS [*Vennerstrom et al.*, 2003] and has been reproduced by multifluid MHD and hybrid models [e.g., *Brain et al.*, 2010; *Najib et al.*, 2011; *Dong et al.*, 2015a; *Modolo et al.*, 2005].

## 4.1. Investigation of the Spatial Resolution

The most complete and accurate global 3-D multispecies single-fluid simulation of the Martian ionized environment has been developed by *Ma et al.* [2004]. It has a varying radial resolution ranging from 10 km in the ionosphere to 630 km in the solar wind, as the multifluid MHD models developed by the same group [*Najib et al.*, 2011]. Mars ionosphere is a key region which represents a conductive obstacle to the solar wind and contributes significantly to the total escape of the ionized planetary particles. An accurate description of this region is required to realistically describe the solar wind-Mars interaction. In the photoequilibrium region of the ionosphere; the plasma scale height is essentially the same as the neutral scale height which ranges from 7 to 50 km (Table 1). Kinetic models are computationally expensive and a full 3-D simulation of the global Martian environment can not yet be performed with a resolution of 10 km. Different solutions have been proposed to reduce the computational resources required for a kinetic simulation run. *Kallio et al.* [2010] used a hierarchical Cartesian grid, but their lowest resolution close to the obstacle is still 180 km, which forces them to introduce a fluid ion background to mimic the ionosphere. More recently, the same group has developed a 3-D global spherical hybrid model for Venus [*Dyadechkin et al.*, 2013], with a minimum radial resolution of 200 km. The model gives a promising result but is not yet applied to the Mars-solar wind interaction. *Boesswetter et al.* [2010] used a Moving Mesh Algorithm with a curvilinear grid, a so-called fish-eye grid, allowing to have a spatial resolution of 76–130 km per cell around the boundary obstacle. The same group has developed an Adaptive Mesh Refinement model for Mercury, Titan, and comets [*Müller et al.*, 2011] and was able to reach 100 km resolution in the finest grid for Mercury. *Brecht and Ledvina* [2012] used a spherical grid to resolve the ionospheric chemistry with a radial resolution of 10 km but compute the currents and the electromagnetic fields evolution on a Cartesian grid of 150 km resolution. A multigrid version of our hybrid model has been developed for Ganymede and allows reaching 125 km resolution [*Leclercq et al.*, 2016], but it has not yet been adapted to Mars and could potentially lead to 25 km resolution.

To summarize, kinetic Martian simulations have been performed with minimum spatial resolution between 100 and 200 km. To investigate the influence of the spatial resolution on the simulation results, we performed a simple test. We used our model with a uniform Cartesian grid of different spatial resolutions. RUN C, our simulation reference with a spatial resolution of 80 km, has been rerun with spatial resolutions of $\Delta x = 0.375c/\omega_{pi} = 50$ km (RUN C2), $\Delta x = 0.975c/\omega_{pi} = 130$ km (RUN C3), and $\Delta x = 1.35c/\omega_{pi} = 180$ km (RUN C4).

Figure 4 gives an overview of the differences between the four simulation runs for the total magnetic field and O^+ ion density in the *XZ* plane. The global magnetic structure is similar for the four runs with a clear BS and magnetic pileup region. For the O^+ ion density maps, the conclusion is similar, global patterns are reproduced in the four simulations, particularly the plume-like population in the +E hemisphere and the ion tailward outflow in the −E hemisphere.

However, a few differences can be noticed. A better representation of the dynamic plume is obvious in the finest spatial resolution case due to a better statistics of the O^+ ion (Figures 4g and 4h). The width of the ionosphere, and therefore the size of the effective obstacle, seems also to be correlated with the spatial resolution. The modeled ionosphere of RUN C2 (Figure 4h) is less extended and slightly denser than the RUN C4 ones (Figure 4e), mostly due to a more accurate ionospheric chemistry description on the finer grid. Moreover, small scale structures in the ion outflow tail can be seen on RUN C and RUN C2 while a more uniform tail distribution is simulated with coarser resolutions (RUN C3 and RUN C4). The different tail dynamic between RUN C and RUN C2 is attributed to numerical fluctuations (not seen at other times of the simulation).

Multiple-shock magnetic signatures are clearer on RUN C and RUN C2 (Figures 4c and 4d) with respect to RUN C3 (Figure 4b). But the main difference betweens these runs dwells in the magnetic pileup region. For RUN C4,
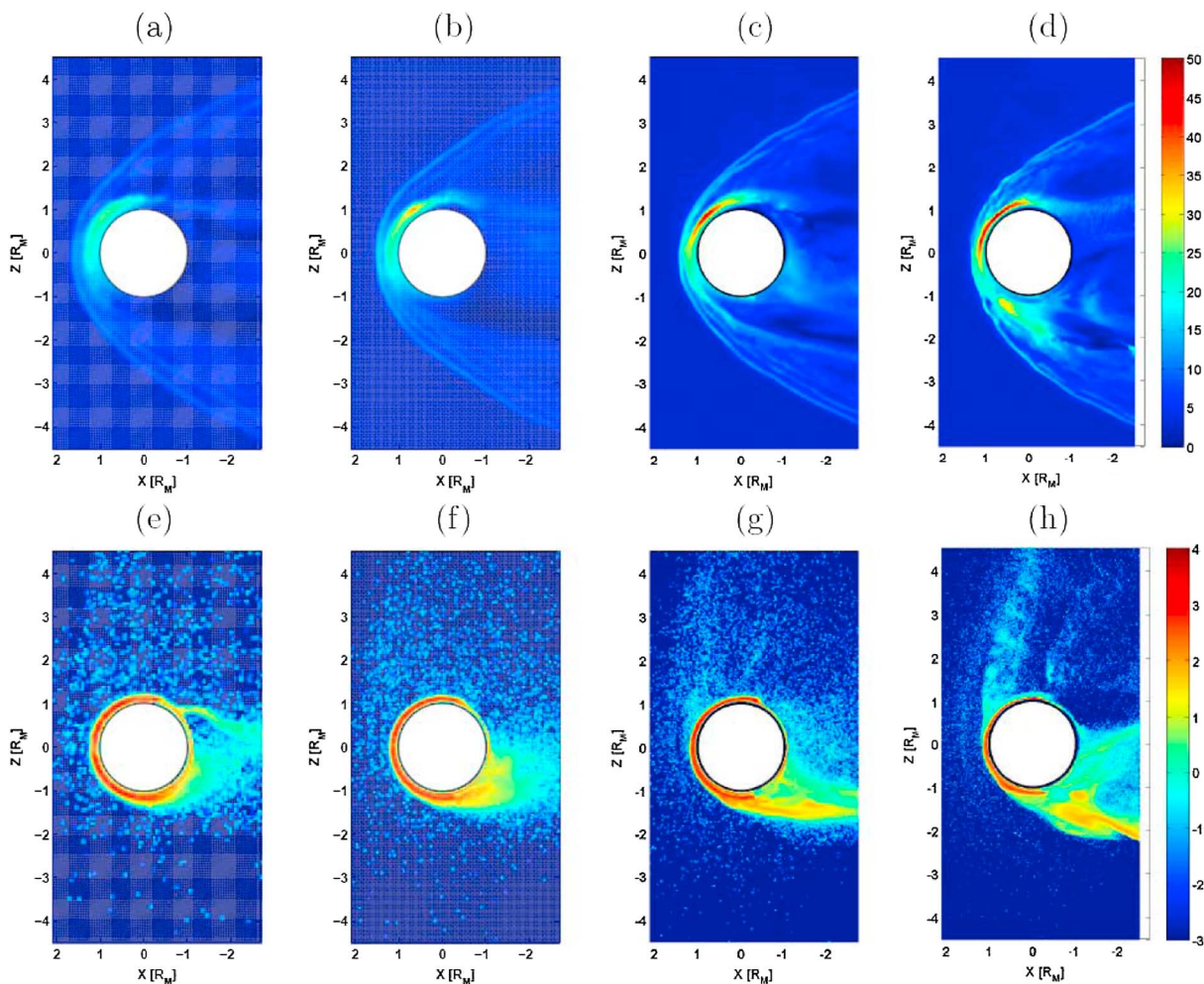
Figure 4. Simulation results of (a, e) RUN C4, (b, f) RUN C3, (c, g) RUN C, and (d, h) RUN C2. The spatial resolution improves from left to right ($\Delta x = 180, 130, 80, and 50$ km). Figures 4a–4d show the total magnetic field (in nT) in the XZ plane while Figures 4e–4h display the O^+ ion number density (in cm^{-3}, log scale) in the same plane, plane containing the convection electric field.

the largest magnetic field reaches 25 nT in this region, while in RUN C and RUN C2 simulated magnetic field intensity reaches 50 nT or more, which is comparable to MGS observations in this region. RUN C3 is an intermediate case with a magnetic field intensity reaching 30–35 nT. This difference is mainly accounted for by two facts. RUN C and RUN C2 describe more properly the ionospheric dynamic with an electron number density of $n_e \sim 10^5$ cm^{-3} denser than in RUN C3 and RUN C4 (few 10^4 cm^{-3}), suggesting a less conducting ionosphere. The pressure balance is better conserved at the ionopause for RUN C and RUN C2 (not shown). Moreover, the magnetic field in the pileup boundary derives from the integration of Ampère's law which involves a spatial partial derivative of the electric field. A finer grid resolution gradients means that gradient and partial derivatives should be better described.

4.2. Boundary Positions

To investigate the influence of the spatial resolution of the solar activity and of the presence of a suprathermal corona on the BS and MPB positions, we compare these boundaries detected automatically in the simulation with their average positions deduced from MGS observations (Figure 5).

Bow shock. The average position of the BS position determined from MGS observations is represented by the dashed black line in Figure 5a, while the grey-shaded area indicates the variation of the average BS position [*Edberg et al.*, 2008]. In order to compare the simulated BS position to MGS observations, an automatic detection criterion has been used. For a given Z value, we search along the X axis the position where the magnitude of the magnetic field exceeds 5 nT. The first value (starting from the solar wind toward the planet, i.e., following the $-X_{MSO}$ direction) is identified as the BS location. A criterion based on pressure balance between thermal
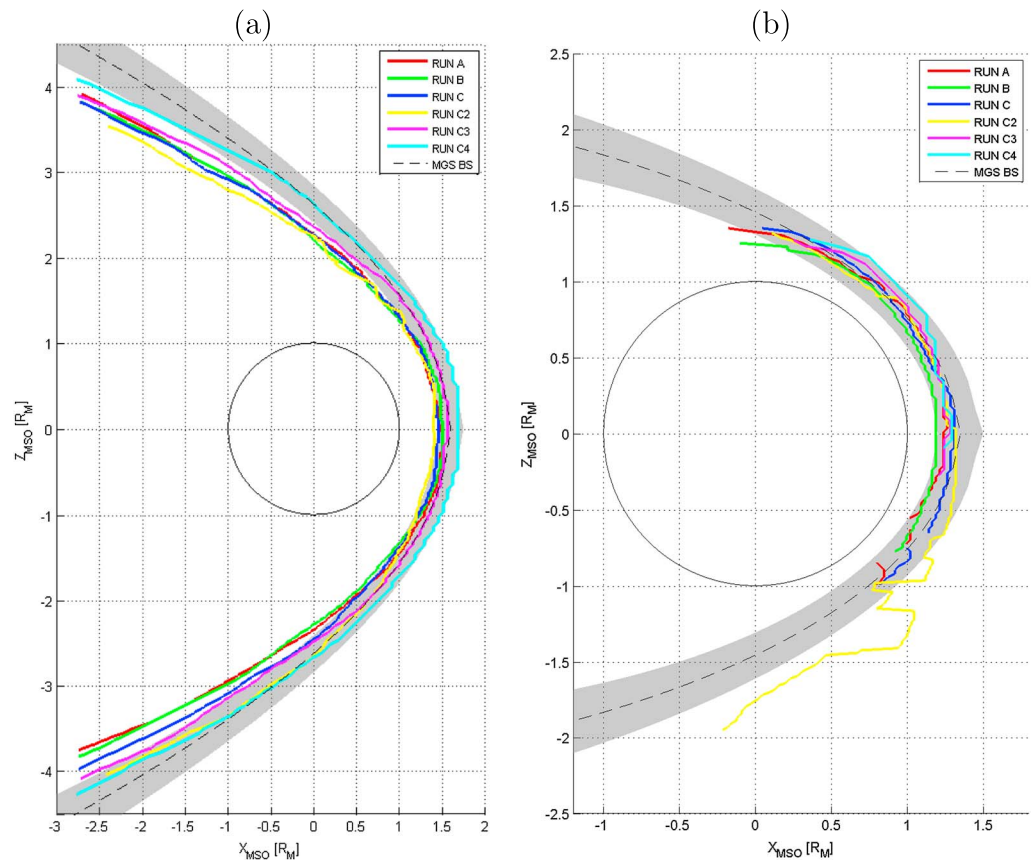
Figure 5. Comparison of the (a) Bow Shock and (b) IMB position for the different simulations (colored solid lines) and average positions deduced from MGS observations (dashed grey line and shaded area representing the uncertainty of the fit to observations).

and dynamic pressures leads to a very similar result on the subsolar region but fails on the outer flanks. Indeed, on the flank, the magnetosheath plasma is reaccelerated flankward/tailward and a simple pressure form is usually poorly fulfilled.

All BS locations are globally in good agreement with the observed average BS position. Simulated BS seems to be less open than the average BS. One explanation relies on the Alfven Mach cone angle which is smaller in the simulation than the average one, due to a slightly faster than usual solar wind used in the simulation (485 km/s instead of $\sim$ 400 km/s in average at Mars).

For RUN A and RUN B, BS positions (red and green curves) are basically identical. Therefore, the suprathermal corona does not affect significantly the BS location at minimum solar activity. The subsolar position of the BS is located at $X = 1.5R_M$. The average subsolar standoff distance determined from MGS observations vary between $1.58 \pm 0.18R_M$ and $1.64 \pm 0.08R_M$ [*Edberg et al.*, 2008; *Vignes et al.*, 2000]. The simulated BS location is slightly closer to the planet than the observations.

The subsolar position for RUN C is $\sim$1.45 R_M, slightly closer to the planet than for RUN B, suggesting a very marginal effect of the solar activity on this position. BS position in the terminator (+E and −E hemispheres) differs by $0.05-0.2\,R_M$ between RUN B and RUN C. However, the mass loading being more important for RUN C, a larger asymmetry of the BS is seen.

RUN C and RUN C2 essentially simulate the same BS location within 0.05 R_M in the +E hemisphere and in the subsolar region. On the −E hemisphere ($-Z_{MSO}$) the BS is significantly farther away for RUN C2 which can be explained by the temporal patchy structure displayed in Figures 4d and 4h. This structure pushed away the BS.

RUN C, RUN C3, and RUN C4 have significant differences on BS locations. When the simulations have a coarse spatial resolution, the BS is found farther away from the obstacle. For RUN C4 the subsolar position of the BS

is at ∼1.67 R_M. With a degraded resolution the ionosphere (obstacle) is more extended since the plasma scale height is much smaller than the spatial resolution.

All simulated BS positions are slightly closer to the planet than the observed average BS location which can be induced by two factors. First of all, MGS data cover a wide range of upstream plasma parameters while all simulations in this paper were performed with a solar wind dynamic pressure slightly stronger than the typical quiet conditions. Moreover, simulations do not take into account crustal fields which have been identified to play an important role in the location of the MPB as well as of the BS [*Edberg et al.*, 2008].

Magnetic pileup boundary. The same identification technique is applied to the simulation results to detect the location of the simulated magnetic pileup boundary. The criterion is still based on the magnitude of the magnetic field. In the case of the MPB we look for values larger than 20 nT. The simulated MPB profile is incomplete because the 20 nT threshold cannot be fulfilled everywhere in the simulation, but the reconstructed MPB profile remains extended enough to compare to MGS observations. The average standoff distance of the MPB vary between 1.25 ± 0.03 R_M and 1.33 ± 0.15 R_M [*Trotignon et al.*, 2006; *Edberg et al.*, 2008]. As shown in Figure 5b, all simulated MPB positions are found within the range of observed position of the MPB.

RUN A and B have the closest MPB with a subsolar position at 1.2–1.25R_M. The position of the boundary for the two simulations are very close to each other and the presence of a suprathermal corona does not seem to play an important role on the location of the MPB.

For RUN C and RUN C2 the MPB has almost the same subsolar position (1.31 R_M) and presents similar shapes except for −Z_{MSO} hemisphere where the MPB is more disturbed and pushed farther from the planet in RUN C2. Here again, this discrepancy between RUN C and RUN C2 can be attributed to a magnetic pileup forming upstream of patchy ionospheric structure moving on the flank and tailward.

RUN C3 and RUN C4 suggest a position of the MPB close to the subsolar region at 1.29R_M, which is quite comparable to the average standoff distance observed by MGS and Phobos 2.

The presence of the crustal fields might be more important accordingly to the MGS results [*Edberg et al.*, 2008].

4.3. O⁺ Ion Escape Rate

Global escape rates can be reconstructed from simulations and observational measurements. Plasma escape rates derived from published simulations with different models vary by a factor 20 for similar input conditions [*Brain et al.*, 2010]. For a various range of solar wind and solar radiation conditions, differences can reach over 2 orders of magnitudes [e.g., *Brecht and Ledvina*, 2010; *Ma and Nagy*, 2007; *Modolo et al.*, 2005; *Kallio and Janhunen*, 2002].

Observational data do not suggest a clearer picture of the total escape rates. The estimates differ by 2 orders of magnitude [e.g., *Lundin et al.*, 1989; *Verigin et al.*, 1991; *Barabash et al.*, 2007; *Fränz et al.*, 2010; *Nilsson et al.*, 2011]. These estimates depend on the location of the measurements and on physical processes contributing to the plasma loss, or the instrumentation, the geometrical assumptions used to derived the global escape rate from local measurements, and many other factors. *Dubinin et al.* [2011] and *Lundin* [2011] provide a good review of the global escape rates deduced from Mars Express and former Martian missions. With the arrival of MAVEN, the determination of the escape rate from the upper atmosphere to space at the present epoch is now revisited with complete instrumentation packages dedicated to answer to this question [*Jakosky et al.*, 2015; *Brain et al.*, 2015; *Dong et al.*, 2015, 2015a].

To better understand the impact of the spatial resolution, of the solar activity and of the neutral corona on the global O^+ escape rates, we compare results from the different simulations using different methods to reconstruct the simulated escape rate. Results of this calculation are summarized in Figure 6.

Global escape rates were computed from a snapshot at the end of each simulation. Three methods are used to compute the escape rates: (1) at the outer boundary of the simulation (circle symbol), (2) at a spherical shell centered on the planet with a radius of 2.06 R_M (asterisk symbol), and (3) at a spherical shell centered on the planet with a radius of 1.35 R_M (diamond symbol). The escape rates displayed in Figure 6 correspond to the total net O⁺ escape balance. To minimize the effect of the numerical fluctuations, intrinsic to the simulation, escape rates have been averaged over a 400 km thickness for the methods using a spherical shell surface and over 5Δx for the method using the outer boundary of the domain.

Simulated escape rate estimates span values between 0.2 and 3.7×10^{24} ions s⁻¹. These estimates are consistent with estimates deduced from observations [e.g., *Brain et al.*, 2015], which include all ions above 30 eV, and
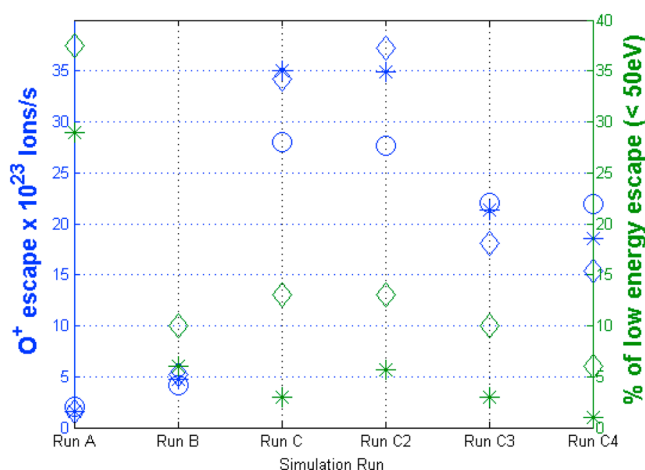
Figure 6. O$^+$ ion escape from different integration surfaces (diamond: spherical shell at the altitude of 1200 km; asterisk: shell at 3600 km; circle: the outer simulation domain) and for the different simulation runs (blue symbols). Green symbols represent the contributions of the lower energy population to the total escape.

other global simulations [e.g., *Ma and Nagy*, 2007; *Dong et al.*, 2015a]. For a given run, the reconstructed escape rate from the three methods varies by 18 to 36%, which confirms the quasi-stationarity of the simulation.

RUN A and RUN B results differ by a factor 2. The suprathermal oxygen corona account for half of the production of escaping ions at solar minimum. RUN B and RUN C results differ by a factor of ∼7 which accounts for the effect of the solar activity (maximum versus minimum) upon the total escape, even if it is not possible to separate the respective role of the neutral corona and of the solar EUV intensity. RUN C and RUN C2 estimated escape rate differs by less than 10%. It confirms that a simulation with a $\Delta x = 80$ km provides a similar description of the Martian environment than a simulation with $\Delta x = 50$ km.

When the spatial resolution is degraded (RUN C3 and RUN C4), O$^+$ escape rates are decreased by ∼25%. The difference is due to the coarser description of the ionospheric region. The contribution of escaping ion O$^+$ produced by the suprathermal oxygen corona is not expected to be altered since the sale height of the neutral profile (Table 1) is of the order of the spatial resolution.

Nilsson et al. [2012] have estimated the tailward flux escape inside the nominal Induced Magnetospheric Boundary as a function of the tail distance. The average value is 1.1×10^{24} s^{-1}, while the total escape is estimated to be equal to 2.2×10^{24} s^{-1}. *Nilsson et al.* [2012] have also separated the contribution from the low- and high-energy components (ions below and above 50 eV). Figure 6 from *Nilsson et al.* [2012] shows that at $X \sim 1.35\, R_M$ about 40–45% of the total escape occur at low energy (< 50 eV), while at $X \sim 2.1\, R_M$ the low-energy ion escape rate falls to 20–25%.

The kinetic formalism of the simulation model allows to separate contributions from low- and high-energy components. The contribution of the low-energy component for the different simulations and ion flux for the different methods of integration of the escape rate are reported in Figure 6. For RUN A, the low-energy component contribution to the escaping flux represents ∼30–37%, while for RUN B it falls to ∼5–10%. This is consistent with the idea that ions produced by the suprathermal oxygen corona are created relatively far away from the planet and are submitted to an important convection electric field which quickly accelerates these ions above the 50 eV detection threshold.

For RUN C the low-energy component of the O$^+$ escape represents ∼3–13% of the total escape. Ions are escaping mostly from two simulation planes: the $-X_{MSO}$ and the $+Z_{MSO}$ (+E hemisphere) exit planes. Ions leaving the $+Z_{MSO}$ simulation plane contributes to 45% of the total escape (the O$^+$ ions plume). In the plume the energy of the escaping ions is much larger than 50 eV. Keeping constant the contribution of the plume for the different methods of integration of the escape rate, the simulated low-energy escape component of the tailward outflow contributes to ∼25% of the tailward flow at $X = 1.35 R_M$ and ∼6% at $X = 2.03 R_M$. It is slightly below the percentage obtained from observational data. Numerical fluctuations of the simulated electric field might contribute to artificially accelerate the plasma.

5. Summary and Conclusion

An improved version of the three-dimensional multispecies hybrid simulation model developed by *Modolo et al.* [2005] has been presented in this paper. This new version of this code, called LatHyS, is parallelized and a realistic description of the ionosphere is included. The parallelization is based on a domain decomposition to be able to track about 1.3 billions of particles on a $320 \times 608 \times 608$ mesh during 18 000 time steps. This modeling effort allows us to describe the Mars-solar wind interaction on a uniform Cartesian grid of 50 km resolution which is, up to now, the finest resolution achieved for a global kinetic model. This forefront paral-lelization development has been carried out in a generic way such that the LatHyS model is now applied to several solar system objects, Mercury [*Richer et al.*, 2012], Ganymede [*Leclercq et al.*, 2016], and the Earth [*Turc et al.*, 2015]. In addition to this technical improvement, the hybrid simulation model has been improved to take into account most of the physical processes involved in the Mars-solar wind interaction. Crustal fields are not included in the present results and will be addressed in a future paper. The strengths of this model are as follows: (1) a kinetic description for ions, including Hall term, Larmor radius effects; (2) a multispecies descrip-tion (6 ion species); (3) two electronic fluids (for solar wind and planetary electrons); (4) local ion production from three ionization processes (photoioniozation, electron impact ionization, and charge exchange); (5) a realistic ionosphere described by a simplified set of chemical equations; (6) a drag force term included in the equations of ionic motion which describe the ion-neutral collisions in the ionosphere; and (7) the effective ionospheric conductivity computed locally.

In this paper, a parametric study is presented in order to determine the influence of the spatial resolution on the simulation results and particularly on the location of the main plasma boundaries and on the total escape. Simulation runs with resolution of $\Delta x = 50$ km (RUN C2), $\Delta x = 80$ km (RUN C), $\Delta x = 130$ km (RUN C3), and $\Delta x = 180$ km (RUN C4) have been performed. Although the global patterns are relatively similar for the different runs, the finest grid simulations (RUN C and RUN C2) display clearly more details of the plasma density, provide a better representation of the ionosphere, and suggest a stronger magnetic pileup compared to coarser spatial resolution. The BS and the MPB positions are all within the variation of the average observed positions. However, the coarser resolution induces a simulated BS location slightly farther from the planet than the refined grid simulations. Due to a better description of the ionosphere, plasma O^+ escape is larger by ~25% in the case of refined grid simulation with respect to coarser resolution simulation.

While the suprathermal oxygen population does not contribute to the plasma boundaries, it accounts for half of the production of escaping ions. We computed the O^+ escape rate with three different methods (from spheres at two distances from the planet and from the limits of the simulation box) and showed that a large fraction of escaping ions originated from below 1200 km in altitude. The solar EUV flux (and the corresponding Martian corona) do not impact significantly on the plasma boundaries location. However, the total O^+ ion escape is found to change by a factor ~7 from minimum to maximum solar activities.

References

Acuna, M. H., et al. (1999), Global distribution of crustal magnetization discovered by the Mars Global Surveyor MAG/ER Experiment, *Science*, *284*, 790–793, doi:10.1126/science.284.5415.790.
Albee, A. L., R. E. Arvidson, F. Palluconi, and T. Thorpe (2001), Overview of the Mars Global Surveyor mission, *J. Geophys. Res.*, *106*, 23,291–23,316, doi:10.1029/2000JE001306.
Anderson, D. E. Jr., and C. W. Hord (1971), Mariner 6 and 7 ultraviolet spectrometer experiment: Analysis of hydrogen Lyman-alpha data, *J. Geophys. Res.*, *76*, 6666–6673, doi:10.1029/JA076i028p06666.
Banks, P., and G. Kockarts (1973), *Aeronomy*, Acad. Press, New York, London.
Barabash, S., A. Fedorov, R. Lundin, and J.-A. Sauvaud (2007), Martian atmospheric erosion rates, *Science*, *315*, 501–503, doi:10.1126/science.1134358.
Bertucci, C., et al. (2003), Magnetic field draping enhancement at the Martian magnetic pileup boundary from Mars global surveyor observations, *Geophys. Res. Lett.*, *30*, 1099, doi:10.1029/2002GL015713.
Birdsall, C., and A. Langdon (2004), *Plasma Physics via Computer Simulation, Series in Plasma Physics*, 504 pp., CRC Press, London.
Boesswetter, A., H. Lammer, Y. Kulikov, U. Motschmann, and S. Simon (2010), Non-thermal water loss of the early Mars: 3D multi-ion hybrid simulations, *Planet. Space Sci.*, *58*, 2031–2043, doi:10.1016/j.pss.2010.10.003.
Bößwetter, A., et al. (2007), Comparison of plasma data from ASPERA-3/Mars-Express with a 3-D hybrid simulation, *Ann. Geophys.*, *25*, 1851–1864, doi:10.5194/angeo-25-1851-2007.
Bougher, S. W., S. Engel, R. G. Roble, and B. Foster (2000), Comparative terrestrial planet thermospheres 3. Solar cycle variation of global structure and winds at solstices, *J. Geophys. Res.*, *105*, 17,669–17,692, doi:10.1029/1999JE001232.
Bougher, S. W., J. M. Bell, J. R. Murphy, M. A. Lopez-Valverde, and P. G. Withers (2006), Polar warming in the Mars thermosphere: Seasonal variations owing to changing insolation and dust distributions, *Geophys. Res. Lett.*, *33*, L02203, doi:10.1029/2005GL024059.
Bougher, S. W., P.-L. Blelly, M. Combi, J. L. Fox, I. Mueller-Wodarg, A. Ridley, and R. G. Roble (2008), Neutral upper atmosphere and ionosphere modeling, *Space Sci. Rev.*, *139*, 107–141, doi:10.1007/s11214-008-9401-9.
Braginskii, S. (1965), *Transport Processes in Plasma, Reviews of Plasma Physics, Consultants Bureau*, pp. 240–265, New York.

Brain, D., et al. (2010), A comparison of global models for the solar wind interaction with Mars, *Icarus*, *206*, 139–151, doi:10.1016/j.icarus.2009.06.030.

Brain, D. A., et al. (2015), The spatial distribution of planetary ion fluxes near Mars observed by Maven, *Geophys. Res. Lett.*, *42*(21), 9142–9148, doi:10.1002/2015GL065293.

Brecht, S. H., and S. A. Ledvina (2010), The loss of water from Mars: Numerical results and challenges, *Icarus*, *206*, 164–173, doi:10.1016/j.icarus.2009.04.028.

Brecht, S. H., and S. A. Ledvina (2012), Control of ion loss from Mars during solar minimum, *Earth, Planets, and Space*, *64*, 165–178, doi:10.5047/eps.2011.05.037.

Chanteur, G. M., E. Dubinin, R. Modolo, and M. Fraenz (2009), Capture of solar wind alpha-particles by the Martian atmosphere, *Geophys. Res. Lett.*, *36*, L23105, doi:10.1029/2009GL040235.

Chaufray, J. Y., R. Modolo, F. Leblanc, G. Chanteur, R. E. Johnson, and J. G. Luhmann (2007), Mars solar wind interaction: Formation of the Martian corona and atmospheric loss to space, *J. Geophys. Res.*, *112*, E09009, doi:10.1029/2007JE002915.

Chaufray, J.-Y., et al. (2014), Three-dimensional Martian ionosphere model: II. Effect of transport processes due to pressure gradients, *J. Geophys. Res. Planets*, *119*, 1614–1636, doi:10.1002/2013JE004551.

Chicarro, A., P. Martin, and R. Trautner (2004), The Mars Express mission: An overview, in *Mars Express: The Scientific Payload*, vol. 1240, edited by A. Wilson, pp. 3–13, ESA Spec. Publ., Noordwijk, Netherlands.

Cravens, T. E., J. U. Kozyra, A. F. Nagy, T. I. Gombosi, and M. Kurtz (1987), Electron impact ionization in the vicinity of comets, *J. Geophys. Res.*, *92*, 7341–7353, doi:10.1029/JA092iA07p07341.

Curry, S. M., M. Liemohn, X. Fang, Y. Ma, and J. Espley (2013), The influence of production mechanisms on pick-up ion loss at Mars, *J. Geophys. Res. Space Physics*, *118*, 554–569, doi:10.1029/2012JA017665.

Curry, S. M., J. Luhmann, Y. Ma, M. Liemohn, C. Dong, and T. Hara (2015), Comparative pick-up ion distributions at Mars and Venus: Consequences for atmospheric deposition and escape, *Planet. Space Sci.*, *115*, 35–47, doi:10.1016/j.pss.2015.03.026.

Dong, C., S. W. Bougher, Y. Ma, G. Toth, A. F. Nagy, and D. Najib (2014), Solar wind interaction with Mars upper atmosphere: Results from the one-way coupling between the multifluid MHD model and the MTGCM model, *Geophys. Res. Lett.*, *41*, 2708–2715, doi:10.1002/2014GL059515.

Dong, C., et al. (2015a), Solar wind interaction with the Martian upper atmosphere: Crustal field orientation, solar cycle, and seasonal variations, *J. Geophys. Res. Space Physics*, *120*, 7857–7872, doi:10.1002/2015JA020990.

Dong, C., et al. (2015b), Multifluid MHD study of the solar wind interaction with Mars' upper atmosphere during the 2015 March 8th ICME event, *Geophys. Res. Lett.*, *42*, 9103–9112, doi:10.1002/2015GL065944.

Dong, Y., et al. (2015), Strong plume fluxes at Mars observed by MAVEN: An important planetary ion escape channel, *Geophys. Res. Lett.*, *42*(21), 8942–8950, doi:10.1002/2015GL065346.

Dubinin, E., M. Fraenz, A. Fedorov, R. Lundin, N. Edberg, F. Duru, and O. Vaisberg (2011), Ion energization and escape on Mars and Venus, *Space Sci. Rev.*, *162*, 173–211, doi:10.1007/s11214-011-9831-7.

Dyadechkin, S., E. Kallio, and R. Jarvinen (2013), A new 3-D spherical hybrid model for solar wind interaction studies, *J. Geophys. Res. Space Physics*, *118*, 5157–5168, doi:10.1002/jgra.50497.

Edberg, N. J. T., M. Lester, S. W. H. Cowley, and A. I. Eriksson (2008), Statistical analysis of the location of the Martian magnetic pileup boundary and bow shock and the influence of crustal magnetic fields, *J. Geophys. Res.*, *113*, A08206, doi:10.1029/2008JA013096.

Fang, X., M. W. Liemohn, A. F. Nagy, J. G. Luhmann, and Y. Ma (2010), Escape probability of Martian atmospheric ions: Controlling effects of the electromagnetic fields, *J. Geophys. Res.*, *115*, A04308, doi:10.1029/2009JA014929.

Fox, J. L. (2009), Morphology of the dayside ionosphere of Mars: Implications for ion outflows, *J. Geophys. Res.*, *114*, E12005, doi:10.1029/2009JE003432.

Fränz, M., E. Dubinin, E. Nielsen, J. Woch, S. Barabash, R. Lundin, and A. Fedorov (2010), Transterminator ion flow in the Martian ionosphere, *Planet. Space Sci.*, *58*, 1442–1454, doi:10.1016/j.pss.2010.06.009.

González-Galindo, F., J.-Y. Chaufray, M. A. López-Valverde, G. Gilli, F. Forget, F. Leblanc, R. Modolo, S. Hess, and M. Yagi (2013), Three-dimensional Martian ionosphere model: I. The photochemical ionosphere below 180 km, *J. Geophys.Res. Planets*, *118*, 2105–2123, doi:10.1002/jgre.20150.

Harned, D. S. (1982), Quasineutral hybrid simulation of macroscopic plasma phenomena, *J. Comput. Phys.*, *47*, 452–462, doi:10.1016/0021-9991(82)90094-8.

Harnett, E. M., and R. M. Winglee (2006), Three-dimensional multifluid simulations of ionospheric loss at Mars from nominal solar wind conditions to magnetic cloud events, *J. Geophys. Res.*, *111*, A09213, doi:10.1029/2006JA011724.

Jakosky, B. M., et al. (2015), The Mars Atmosphere and Volatile Evolution (MAVEN) mission, *Space Sci. Rev.*, *195*(1–4), 3–48, doi:10.1007/s11214-015-0139-x.

Kallio, E., and P. Janhunen (2001), Atmospheric effects of proton precipitation in the Martian atmosphere and its connection to the Mars-solar wind interaction, *J. Geophys. Res.*, *106*, 5617–5634, doi:10.1029/2000JA000239.

Kallio, E., and P. Janhunen (2002), Ion escape from Mars in a quasi-neutral hybrid model, *J. Geophys. Res.*, *107*(A3), 1035, doi:10.1029/2001JA000090.

Kallio, E., K. Liu, R. Jarvinen, V. Pohjola, and P. Janhunen (2010), Oxygen ion escape at Mars in a hybrid model: High energy and low energy ions, *Icarus*, *206*, 152–163, doi:10.1016/j.icarus.2009.05.015.

Kallio, E., J.-Y. Chaufray, R. Modolo, D. Snowden, and R. Winglee (2011), Modeling of Venus, Mars, and Titan, *Space Sci. Rev.*, *162*, 267–307, doi:10.1007/s11214-011-9814-8.

Kelley, M. (1989), *The Earth's Ionosphere, Plasma Physics and Electrodynamics, Intl. Geophys. Ser.*, vol. 43, Acad. Press, San Diego, Calif.

Kim, Y. K., et al. (2004), Electron-impact ionization cross section database (version 3.0). [Available at http://physics.nist.gov/ionxsec.]

Krasnopolsky, V. A. (2002), Mars' upper atmosphere and ionosphere at low, medium, and high solar activities: Implications for evolution of water, *J. Geophys. Res.*, *107*, 5128, doi:10.1029/2001JE001809.

Leclercq, L., R. Modolo, F. Leblanc, S. Hess, and M. Mancini (2016), 3D magnetospheric parallel hybrid multi-grid method applied to planet-plasma interactions, *J. Comput. Phys.*, *309*, 295–313, doi:10.1016/j.jcp.2016.01.005.

Ledvina, S. A., Y.-J. Ma, and E. Kallio (2008), Modeling and simulating flowing plasmas and related phenomena, *Space Sci. Rev.*, *139*, 143–189, doi:10.1007/s11214-008-9384-6.

Lillis, R. J., et al. (2015), Characterizing atmospheric escape from Mars today and through time, with MAVEN, *Space Sci. Rev.*, *195*, 357–422, doi:10.1007/s11214-015-0165-8.

Lipatov, A. S., E. C. Sittler, R. E. Hartle, J. F. Cooper, and D. G. Simpson (2011), Background and pickup ion velocity distribution dynamics in Titan's plasma environment: 3D hybrid simulation and comparison with CAPS T9 observations, *Adv. Space Res.*, *48*, 1114–1125, doi:10.1016/j.asr.2011.05.026.

Lundin, R. (2011), Ion acceleration and outflow from Mars and Venus: An overview, *Space Sci. Rev.*, *162*, 309–334, doi:10.1007/s11214-011-9811-y.

Lundin, R., H. Borg, B. Hultqvist, A. Zakharov, and R. Pellinen (1989), First measurements of the ionospheric plasma escape from Mars, *Nature*, *341*, 609–612, doi:10.1038/341609a0.

Lundin, R. et al. (2004), Solar wind-induced atmospheric erosion at Mars: First results from ASPERA-3 on Mars express, *Science*, *305*, 1933–1936, doi:10.1126/science.1101860.

Ma, Y., A. F. Nagy, K. C. Hansen, D. L. Dezeeuw, T. I. Gombosi, and K. G. Powell (2002), Three-dimensional multispecies MHD studies of the solar wind interaction with Mars in the presence of crustal fields, *J. Geophys. Res.*, *107*, 1282, doi:10.1029/2002JA009293.

Ma, Y., A. F. Nagy, I. V. Sokolov, and K. C. Hansen (2004), Three-dimensional, multispecies, high spatial resolution MHD studies of the solar wind interaction with Mars, *J. Geophys. Res.*, *109*, A07211, doi:10.1029/2003JA010367.

Ma, Y., X. Fang, C. T. Russell, A. F. Nagy, G. Toth, J. G. Luhmann, D. A. Brain, and C. Dong (2014), Effects of crustal field rotation on the solar wind plasma interaction with Mars, *Geophys. Res. Lett.*, *41*, 6563–6569, doi:10.1002/2014GL060785.

Ma, Y.-J., and A. F. Nagy (2007), Ion escape fluxes from Mars, *Geophys. Res. Lett.*, *34*, L08201, doi:10.1029/2006GL029208.

Matthews, A. P. (1994), Current advance method and cyclic leapfrog for 2D multispecies hybrid plasma simulations, *J. Comput. Phys.*, *112*, 102–116, doi:10.1006/jcph.1994.1084.

Message Passing Interface Forum (2012), MPI: A Message-Passing Interface Standard, Version 3.0. High Performance Computing Center Stuttgart (HLRS). [Available at http://www.unixer.de/~htor/publications/.]

Modolo, R., and G. M. Chanteur (2008), A global hybrid model for Titan's interaction with the Kronian plasma: Application to the Cassini Ta flyby, *J. Geophys. Res.*, *113*, A01317, doi:10.1029/2007JA012453.

Modolo, R., G. M. Chanteur, E. Dubinin, and A. P. Matthews (2005), Influence of the solar EUV flux on the Martian plasma environment, *Ann. Geophys.*, *23*, 433–444, doi:10.5194/angeo-23-433-2005.

Modolo, R., G. M. Chanteur, E. Dubinin, and A. P. Matthews (2006), Simulated solar wind plasma interaction with the Martian exosphere: Influence of the solar EUV flux on the bow shock and the magnetic pile-up boundary, *Ann. Geophys.*, *24*, 3403–3410, doi:10.5194/angeo-24-3403-2006.

Modolo, R., G. M. Chanteur, and E. Dubinin (2012), Dynamic Martian magnetosphere: Transient twist induced by a rotation of the IMF, *Geophys. Res. Lett.*, *39*, L01106, doi:10.1029/2011GL049895.

Müller, J., S. Simon, U. Motschmann, J. Schüle, K.-H. Glassmeier, and G. J. Pringle (2011), A.I.K.E.F.: Adaptive hybrid model for space plasma simulations, *Comput. Phys. Commun.*, *182*, 946–966, doi:10.1016/j.cpc.2010.12.033.

Najib, D., A. F. Nagy, G. Tóth, and Y. Ma (2011), Three-dimensional, multifluid, high spatial resolution MHD model studies of the solar wind interaction with Mars, *J. Geophys. Res.*, *116*, A05204, doi:10.1029/2010JA016272.

Nilsson, H., N. J. T. Edberg, G. Stenberg, S. Barabash, M. Holmström, Y. Futaana, R. Lundin, and A. Fedorov (2011), Heavy ion escape from Mars, influence from solar wind conditions and crustal magnetic fields, *Icarus*, *215*, 475–484, doi:10.1016/j.icarus.2011.08.003.

Nilsson, H., G. Stenberg, Y. Futaana, M. Holmström, S. Barabash, R. Lundin, N. J. T. Edberg, and A. Fedorov (2012), Ion distributions in the vicinity of Mars: Signatures of heating and acceleration processes, *Earth, Planets, and Space*, *64*, 135–148, doi:10.5047/eps.2011.04.011.

Poppe, A. R., and S. M. Curry (2014), Martian planetary heavy ion sputtering of Phobos, *Geophys. Res. Lett.*, *41*, 6335–6341, doi:10.1002/2014GL061100.

Rees, M. H. (1989), *Physics and Chemistry of the Upper Atmosphere*, Cambridge Univ. Press, Cambridge.

Richards, P. C., J. A. Fennelly, and D. G. Torr (1994), EUVAC: A solar EUV flux model for aeronomic calculations, *J. Geophys. Res.*, *99*(A5), 8981–8992, doi:10.1029/94JA00518.

Richer, E., R. Modolo, G. M. Chanteur, S. Hess, and F. Leblanc (2012), A global hybrid model for Mercury's interaction with the solar wind: Case study of the dipole representation, *J. Geophys. Res.*, *117*, A10228, doi:10.1029/2012JA017898.

Riousset, J. A., C. S. Paty, R. J. Lillis, M. O. Fillingim, S. L. England, P. G. Withers, and J. P. M. Hale (2013), Three-dimensional multifluid modeling of atmospheric electrodynamics in Mars' dynamo region, *J. Geophys. Res. Space Physics*, *118*, 3647–3659, doi:10.1002/jgra.50328.

Schunk, R. W., and A. F. Nagy (2004), *Ionospheres*, Cambridge Univ. Press, Cambridge, U. K.

Simon, S., A. Bößwetter, T. Bagdonat, U. Motschmann, and K.-H. Glassmeier (2006), Plasma environment of Titan: A 3-D hybrid simulation study, *Ann. Geophys.*, *24*, 1113–1135, doi:10.5194/angeo-24-1113-2006.

Spreiter, J. R., and S. S. Stahara (1980), A new predictive model for determining solar wind-terrestrial planet interactions, *J. Geophys. Res.*, *85*, 6769–6777, doi:10.1029/JA085iA12p06769.

Stancil, P. C., D. R. Schultz, M. Kimura, J.-P. Gu, G. Hirsch, and R. J. Buenker (1999), Charge transfer in collisions of O^+ with H and H^+ with O, *Astron. Astrophys. Suppl.*, *140*, 225–234, doi:10.1051/aas:1999419.

Stebbings, R. F., A. C. H. Smith, and H. Ehrhardt (1964), Charge transfer between oxygen atoms and O^+ and H^+ ions, *J. Geophys. Res.*, *69*, 2349–2355, doi:10.1029/JZ069i011p02349.

Terada, N., H. Shinagawa, T. Tanaka, K. Murawski, and K. Terada (2009), A three-dimensional, multispecies, comprehensive MHD model of the solar wind interaction with the planet Venus, *J. Geophys. Res.*, *114*, A09208, doi:10.1029/2008JA013937.

Trotignon, J. G., C. Mazelle, C. Bertucci, and M. H. Acuña (2006), Martian shock and magnetic pile-up boundary positions and shapes determined from the Phobos 2 and Mars Global Surveyor data sets, *Planet. Space Sci.*, *54*, 357–369, doi:10.1016/j.pss.2006.01.003.

Turc, L., D. Fontaine, P. Savoini, and R. Modolo (2015), 3D hybrid simulations of the interaction of a magnetic cloud with a bow shock, *J. Geophys. Res. Space Physics*, *120*, 6133–6151, doi:10.1002/2015JA21318.

Valeille, A., M. R. Combi, V. Tenishev, S. W. Bougher, and A. F. Nagy (2010), A study of suprathermal oxygen atoms in Mars upper thermosphere and exosphere over the range of limiting conditions, *Icarus*, *206*, 18–27, doi:10.1016/j.icarus.2008.08.018.

Vennerstrom, S., N. Olsen, M. Purucker, M. H. Acuña, and J. C. Cain (2003), The magnetic field in the pile-up region at Mars, and its variation with the solar wind, *Geophys. Res. Lett.*, *30*, 1369, doi:10.1029/2003GL016883.

Verigin, M. I., et al. (1991), Ions of planetary origin in the Martian magnetosphere (Phobos 2/TAUS experiment), *Planet. Space Sci.*, *39*, 131–137, doi:10.1016/0032-0633(91)90135-W.

Vignes, D., et al. (2000), The solar wind interaction with Mars: Locations and shapes of the bow shock and the magnetic pile-up boundary from the observations of the MAG/ER Experiment onboard Mars Global Surveyor, *Geophys. Res. Lett.*, *27*, 49–52, doi:10.1029/1999GL010703.

Vignes, D., M. H. Cuña, J. E. P. Connerney, D. H. Crider, H. Rème, and C. Mazelle (2002), Factors controlling the location of the Bow Shock at Mars, *Geophys. Res. Lett.*, *29*, 1328, doi:10.1029/2001GL014513.

Winske, D., et al. (2003), Hybrid simulation codes: Past, present and future — A tutorial, in *Space Plasma Simulation Lecture Notes in Physics*, vol. 615, edited by J. Büchner, C. Dum, and M. Scholer, pp. 136–165, Springer, Berlin.